Experimental Feasibility Study of Confocal Microwave Imaging for Breast Tumor Detection

Elise C. Fear, *Member, IEEE*, Jeff Sill, *Student Member, IEEE*, and Maria A. Stuchly, *Fellow, IEEE*

***Abstract*—Initial experimental verification of confocal microwave imaging for breast tumor detection is described. Simple phantoms, consisting of a PVC pipe and objects representing tumors, are scanned with resistively loaded monopole or horn antennas. Successful reduction of clutter and detection of a variety of two-dimensional objects is demonstrated.**

***Index Terms*—Cancer detection, microwave imaging, experimental verification.**

I. Introduction

CONFOCAL microwave imaging (CMI) for breast cancer detection was first proposed by Hagness *et al.* [1], [2] based on numerical modeling. The CMI technique is relatively simple and avoids the complexity of classical microwave imaging, which involves nonlinear solutions of the inverse problem. Analogous to ground-penetrating radar, reflected signals from antennas placed in different positions are used to infer the locations of significant microwave scatterers. Scattering arises from differences in the dielectric properties of normal breast tissue and malignant lesions [1], [2]. In the planar CMI system introduced in [1] and [2], the patient lies on her back and a single antenna is scanned over the flattened breast. Encouraging results were obtained with three-dimensional (3-D) modeling [2] and a realistic two-dimensional (2-D) breast model based on magnetic resonance imaging (MRI) scans [3]. A cylindrical CMI system was also proposed [4], [5]. The patient lies on her front with the breast extending through a hole in the examination table and immersed in a liquid. Antennas are scanned in a cylindrical or conical pattern around the breast and are separated from the breast by a few millimeters (typically 1 cm). Detection capabilities of both systems are similar [6], while the cylindrical system geometry at present appears more convenient for clinical application.

Previously published research on breast cancer detection with CMI relied on numerical modeling. In this work, we present the results of a simple experimental study aimed at verification of the basic concepts developed with numerical modeling. To avoid unnecessary complications (mostly mechanical), the experiment has been performed in free space rather than in liquids simulating tissues and the immersion liquid. After describing the phantoms and experiments, the signal processing and image formation methods are summarized. Effective methods for converting the measured frequency domain data to the time domain are investigated. Modifications to previously reported image formation algorithms make better use of the information in the experimental data. Results are presented for phantoms containing a variety of objects, ranging from strongly scattering objects to more challenging detection tasks. Images obtained with two different antennas are compared, and system resolution is investigated. The results presented here are expected to apply to a large extent to the planar configuration of CMI as well.

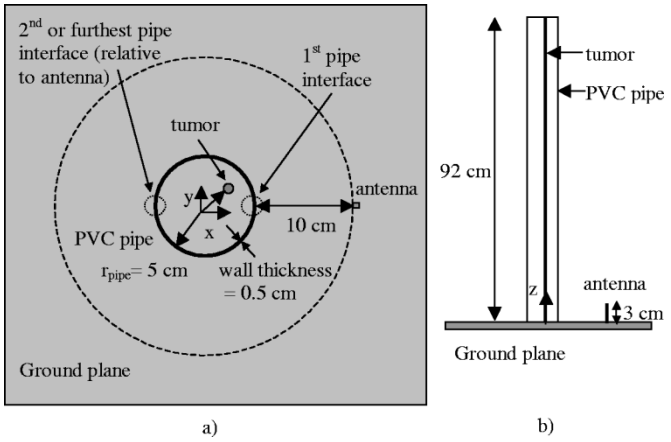

Fig. 1. Test setup with a monopole antenna, PVC pipe and wood dowel tumor. (a) Top-down view. (b) Side view.

II. Experimental System

To investigate tumor detection and localization, as well as the influence of the antenna, the experimental arrangements shown in Figs. 1 and 2 are utilized. The first experiment (Fig. 1) is designed for initial verification of tumor detection and localization in a 2-D plane and incorporates a monopole antenna. To study the feasibility of using a more efficient antenna, the test setup in Fig. 2 is developed. In all experiments, an 8720C vector network analyzer (Agilent Technol., Palo Alto, CA) is connected to the antenna with a 50-Ω coaxial cable. The setup is surrounded with electromagnetic absorbing material to reduce ambient reflections. The antennas illuminate the phantom, and S_{11} is recorded as the frequency is varied from 50 MHz to 20 GHz (monopole) or from 1 to 18 GHz (horn). Data are recorded at 401 frequency points, and 128 measurements are averaged at each frequency. The phantom is rotated in 16 increments of 22.5° to simulate scanning the antenna around the pipe, and reflections are observed after each rotation.

Manuscript received April 4, 2002; revised October 4, 2002. This work was supported by the Natural Sciences and Engineering Research Council of Canada.

E. C. Fear and J. Sill are with the Department of Electrical and Computer Engineering, University of Calgary, Calgary, AB, Canada T2N 1N4 (e-mail: fear@enel.ucalgary.ca).

M. A. Stuchly is with the Department of Electrical and Computer Engineering, University of Victoria, Victoria, BC, Canada V8W 3P6.

Digital Object Identifier 10.1109/TMTT.2003.808630

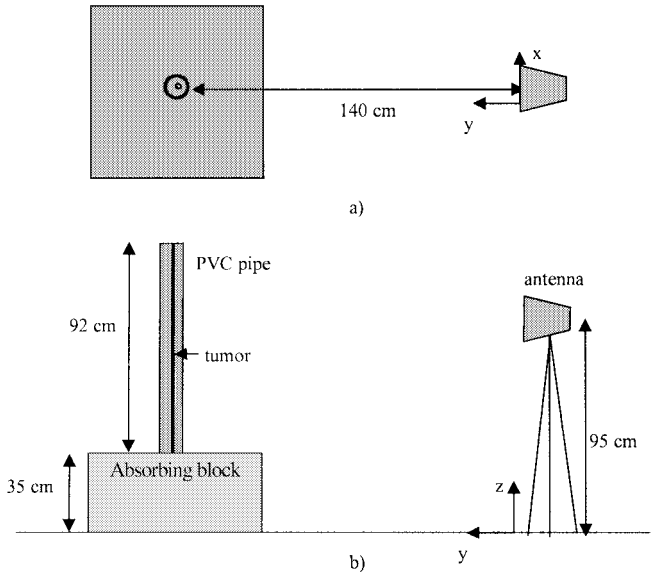

Fig. 2. Test setup with horn antenna, PVC pipe and wood dowel tumor. (a) Top-down view. (b) Side view.

TABLE I
MATERIALS, DIMENSIONS, AND ESTIMATED RELATIVE PERMITTIVITIES OF PHANTOMS

Phantom	Material	Diameter (cm)	Estimated relative permittivity
1	PVC pipe	10	3.3
2	Copper	1.6	-
3	Water	1.6	78
4a	Wood dowel	1.2	2
4b		0.3	
4c		2x1.2 (3.4 cm separation)	
4d		2x1.2 (2.1cm separation)	
5	Wood hemisphere	5	2

The phantom consists of a PVC pipe and various materials simulating the tumor (Table I). In most cases, the lengths of the pipe and objects are much greater than the length of the antenna, and the phantom may be considered 2-D. This assumption is similar to those made with initial simulations of CMI [4]. The dielectric constants are not consistent with the realistic dielectric constants of breast tissues, however, the contrast between air and PVC is similar to the expected contrast between breast tissue and skin. Although dielectric loss is associated with biological tissues (modest for breast tissue, larger for skin and tumor), the PVC pipe is not filled with a lossy material. In an attempt to compensate for the lack of loss, the contrast between the materials representing skin and tumors is reduced. This contrast is, with one exception, lower than the contrast used in simulations of CMI (as estimated from available tissue data).

The first experiment uses a monopole antenna with a Wu-King resistive loading profile, built by soldering together resistors as in [7]. The antenna length is 3 cm, corresponding to a quarter wavelength at 2.5 GHz. However, the frequency used to design the loading profile is 10 GHz, as this higher design frequency is expected to provide improved standing wave ratio and efficiency [8]. This is verified by designing profiles using frequencies of 2.5 and 10 GHz, building the antennas and measuring their performance [9]. The antenna is placed 10 cm from the phantom, as finite-difference time-domain (FDTD) simulations [10] indicate that time signatures of the radiated fields do not change with increased distance from the antenna (i.e., the phantom is illuminated with fields having the same time signatures).

A horn antenna is used in the second experimental arrangement, specifically an EMCO model 3115 double-ridged waveguide antenna (EMC Test Syst., Austin, TX), which is a linearly polarized broad-band antenna designed to operate from 1 to 18 GHz. The gain at a distance of 1 m from the horn varies from 5.6 dBi at 1 GHz to 16.5 dBi at 16 GHz [11]. The E and H plane beamwidths are approximately 60° at 1 GHz, decreasing to 40° at 5 GHz [11]. An appropriate separation between the antenna and phantom is determined by examining reflections from a metal plate placed between 120 and 150 cm from the end of the horn. At distances of 140 cm and greater, the time signatures of the reflections from the plate do not change significantly. The antenna-object separation is larger than expected for the imaging application; a more practical distance will result from both use of an immersion liquid and design of an application-specific antenna.

III. Signal Processing and Image Formation

The measured data are in the frequency domain and must be converted to the time domain for compatibility with the image formation algorithm. A differentiated Gaussian weighting window is applied to the measured data to produce the desired time-domain pulse

$$V(t) = V_0(t - t_0) \cdot e^{-(t-t_0)^2/\tau^2} \tag{1}$$

where V_0 is used to adjust the amplitude of the pulse, $t_0 = 4\tau$ and $\tau = 43$ ps. This pulse has maximum frequency content near 5.24 GHz and full-width half-maximum (FWHM) bandwidth from 1.68 to 10 GHz. For the first few tests (phantoms 2, 3, and 4a), the weighted signals are transformed to the time domain with inverse Fourier transforms. Inverse chirp-z transforms provide flexibility in selection of the time step [12], [13]. Smaller time steps may assist in clutter reduction, which is more important for the less strongly scattering tumor models. To test this hypothesis, results obtained with inverse Fourier and chirp-z transforms are compared for phantom 4a. For the remainder of the data, inverse chirp-z transforms are utilized to convert the frequency domain data to the time domain.

The image reconstruction algorithm introduced in [6] is adapted for the experimental data. Specifically, an additional image is formed to identify the pipe location and this information is used to time-gate the data. First, the signals are calibrated by subtracting the signal received at the antenna without an object present. After calibration, the pipe reflections dominate the signal and must be reduced to permit detection of tumor models inside of the pipe. It is also useful to eliminate reflections that do not originate from the pipe, such as reflections from the absorbers or the environment, by time-gating the data. To determine an appropriate time gate, an image is formed by scanning a synthetic focus through the region bounded by the antenna locations. Prior to focusing, the signals are integrated to

transform the midpoint (in time) of the excitation signal from a zero to a maximum. This is essential for focusing, which relies upon coherent addition of the maxima of signals. The synthetic focus is accomplished by computing the distance between each antenna and the selected focus, converting this to a time delay, and summing the time-delayed data. When the focus is located at the pipe walls, the pipe reflections add together, creating larger responses at these pixel locations. The resulting image contains an outline of the pipe and is filtered to enhance the pipe response and reduce clutter. For the data recorded with the monopole antenna, an adaptive Wiener filter is applied to the image. The size of the region used to compute filter statistics is bounded by 10% of the image size and is determined by growing a region around a randomly selected pixel. For data recorded with the horn antenna, thresholding is used to identify the pipe. After filtering or thresholding, edges are identified, dilated, and connected. The largest group of connected pixels is defined as the pipe, and all other pixels are removed from the image. The pixels located closest to and furthest from each antenna are assumed to represent the first and second pipe interfaces (Fig. 1). To limit the data to reflections from the pipe, the calibrated data arriving before the first pipe reflection and after the second reflection are set to zero. It should be emphasized that identification of pipe location and time gating of data require no intervention by the user.

Once filtering and time gating are complete, the image reconstruction algorithm proceeds as previously described [6]. To reduce the reflection from the pipe, the signals are time shifted to align the dominant reflections in the signal, and the average response of the data set is subtracted from each signal. Radial spreading compensation is applied to account for the $1/r$ decrease in amplitude of the wave as it travels from the source. Finally, the data are integrated and focused. If the focal point is located inside of the pipe, the time delay from each antenna to the focal point is increased to compensate for travel through the pipe. Data are also weighted to emphasize data from antennas located closer to each focal point. The displayed image is the squared result of the focusing step, and is proportional to the field intensity.

To gain insight into each signal processing step, tumor and pipe reflection ratios are calculated. The tumor reflection ratio compares the peak-to-peak reflection from the tumor model with the peak-to-peak reflection from the PVC pipe. The peak-to-peak tumor response is obtained by subtracting measurements of tumor-bearing and tumor-free phantoms. The pipe reflection ratio compares peak-to-peak reflections from second (further) and first (closer) pipe interfaces. The location and size of the tumor response in the image are also assessed. The response size describes the area in the image with greater than half the maximum tumor response value. Tumor location is the location of the maximum response in the image (relative to the center of the pipe). Signal-to-clutter (S/C) ratios, which compare the maximum tumor response to the maximum clutter response in the same image, are also calculated.

IV. Results and Discussion

To demonstrate the need for reduction of reflections from the pipe, Fig. 3 shows signals recorded with the monopole antenna after calibration. Reflections from the first and second pipe interfaces, as well as the wood dowel tumor, are evident. Table II summarizes tumor and pipe reflection ratios for several phantoms. As expected, smaller reflections are obtained as the tumor model decreases in size and as the distance between the antenna and tumor model is increased. Data for the monopole and horn antenna are also compared in Table II, demonstrating that larger relative reflections from both the wood dowel tumor and second pipe interface are obtained with the horn. This implies that, although the tumor reflection is more significant, a more difficult clutter reduction problem exists with the horn antenna.

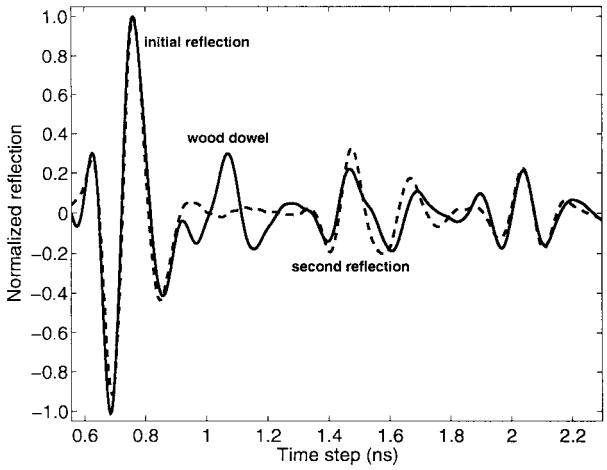

Fig. 3. Reflections from the PVC pipe (dashed line) and the PVC pipe containing a 1.2-cm-diameter wood dowel tumor (solid line). The data are recorded with the monopole antenna.

TABLE II
COMPARISON OF REFLECTIONS FROM PHANTOMS RECORDED WITH MONOPOLE AND HORN ANTENNAS. TUMOR LOCATION IS THE DISTANCE BETWEEN THE WOOD DOWEL TUMOR AND PIPE EDGE CLOSEST TO THE ANTENNA

Antenna	Tumor model			Pipe
	diameter (cm)	location (cm)	reflection ratio (dB)	reflection ratio (dB)
Monopole	1.2	8.1	-18.1	-
Monopole	0.3	8.1	-26.0	-
Monopole	1.2	3.4	-14.7	-12.0
Horn	1.2	3.4	-10.0	-1.7

To test our ability to detect 2-D objects with the monopole antenna, tumor models of various sizes and materials are imaged. Figs. 4–6 provide images, and Table III summarizes S/C ratios and tumor response information. These results demonstrate that the pipe reflections and other clutter signals are successfully reduced, allowing for detection of the tumor models at locations corresponding reasonably well to their physical positions. Comparison of S/C ratios for phantoms 2, 3 and 4a shows that larger ratios are obtained for objects of higher contrast. Results for the phantom containing a 1.2-cm dowel and the two methods of inverse transform are shown in Figs. 4 and 5. Reduced clutter is evident in Fig. 5, resulting in an improved S/C ratio. A smaller time step is selected with the inverse chirp-z approach, allowing for more accurate alignment of reflections and improved canceling of pipe reflections. Next, data for the 1.2-cm wood dowel tumor are acquired with each of two fabrications of the same

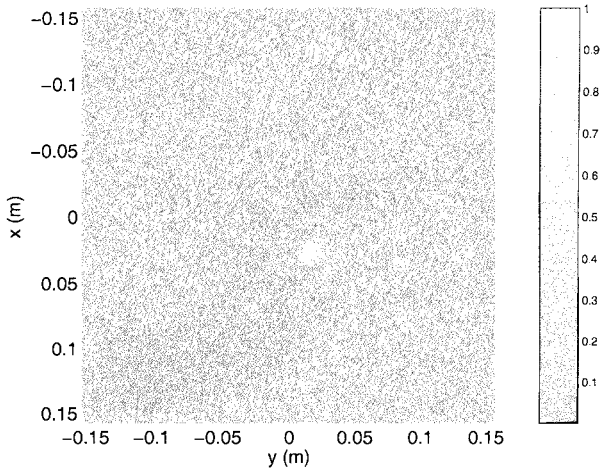

Fig. 4. Image of a 1.2-cm-diameter wood dowel tumor located inside a PVC pipe. The time-domain signals are obtained with inverse Fourier transforms.

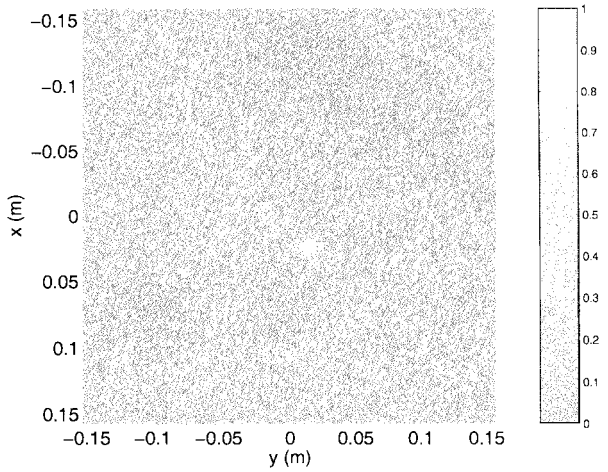

Fig. 5. Image of a 1.2-cm-diameter wood dowel tumor located inside a PVC pipe. The time domain signals are obtained with inverse chirp-z transforms.

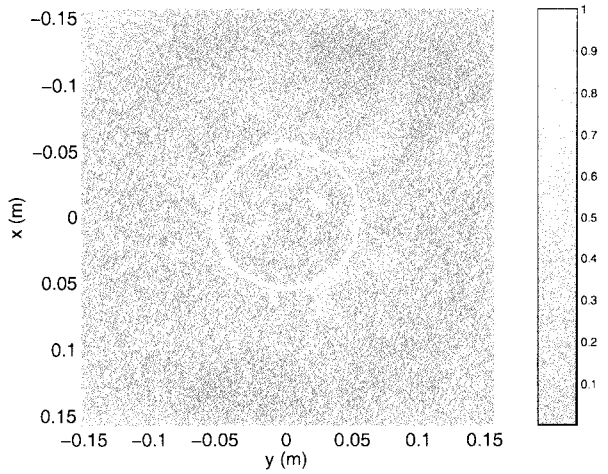

Fig. 6. Image of a wood dowel tumor with a diameter of 3 mm. The white line shows the location of the pipe estimated by the image formation algorithm.

monopole antenna design. Small variations in input impedances of the antennas are noted, however, detection of the wood dowel tumor is successful for both data sets. A larger S/C ratio is obtained with the second data set, primarily due to the incoherent addition of the clutter that results in decreased clutter contribution for this case. Detection of a 3-mm-diameter wood dowel tumor is shown in Fig. 6, demonstrating successful reduction of the pipe reflection and detection of a small diameter object.

TABLE III
DETECTION RESULTS FOR VARIOUS TUMORS. THE VALUES IN BRACKETS INDICATE THE ACTUAL AREAS AND LOCATIONS OF THE TUMORS

Phantom	Tumor model response size (mm^2)	location (cm)	S/C ratio (dB)
2	90 (201)	2.8 (2)	12.2
3	110 (201)	3.0 (3.0)	8.7
4a, FFT	168 (113)	3.2 (3.1)	3.7
4a, chirp	115 (113)	2.9 (3.1)	7.6
4a, chirp, data set 2	119 (113)	2.8 (2.6)	9.2
4b	61 (7)	2.6 (2.8)	2.1
4c	Distance between maxima: 3.8 cm (3.4)		1.5
4d	Distance between maxima: 2.2 cm (2.1)		2.0
5	146 (1963)	1.1 (0.8)	2.7
4a, horn	105 (113)	2.5 (2.8)	4.6

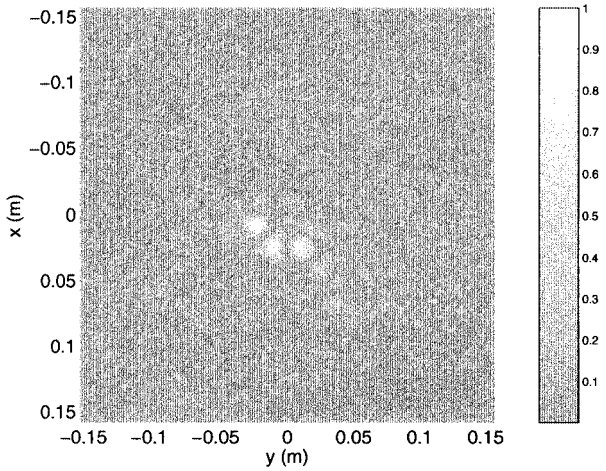

Fig. 7. Image of two wood dowel tumors with 1.2-cm diameter. The centers of the dowels are separated by 3.4 cm, and the dowels are located inside a PVC pipe.

The system resolution is investigated by imaging a phantom containing two 1.2-cm dowels. Images for two separations are shown in Figs. 7 and 8, and the distances between the maximum responses are included in Table III. The objects with center separation of 3.4 cm (edge separation of 2.2 cm) appear as two separate objects. The objects with centers separated by 2.1 cm (0.9-cm separation between edges) appear as a united object. In both cases, greater clutter arises near the two objects, however, this is likely a feature of the presence of two objects rather than coherent addition of reflections unrelated to the tumor models. It is clear that an object is present inside of the PVC pipe, and that responses are more complex than those observed with only one tumor model. For the signal described in (1), the calculated resolution is 1.8 cm. More investigation is required, especially with 3-D objects, however it appears that the system performance is in the range predicted by theory. In spite of resolution on the order of 1 cm, individual wood dowel tumors 3 mm in diameter are detected.

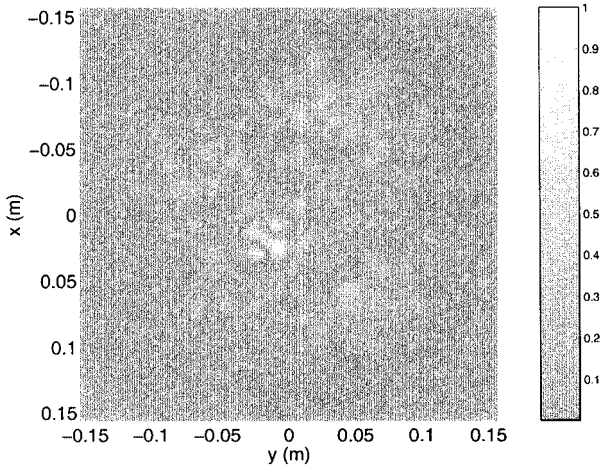

Fig. 8. Image of two wood dowel tumors with 1.2 cm diameter. The separation between the centers is 2.1 cm, and the dowels are located inside a PVC pipe.

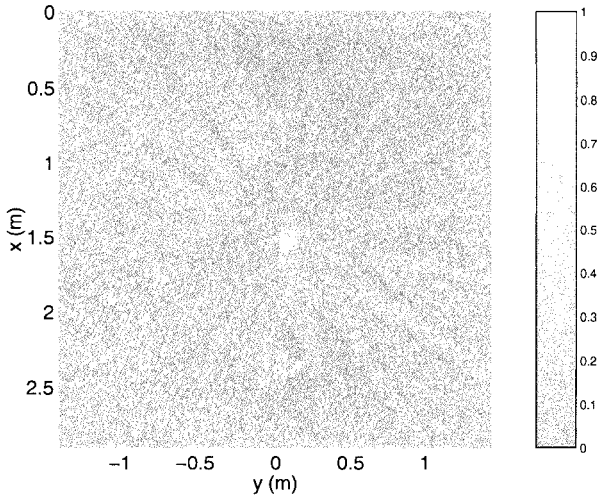

Fig. 9. Image of a 1.2-cm-diameter wood dowel tumor inside of the PVC pipe. The data are obtained with the horn antenna.

To test our ability to detect 3-D objects, a wooden hemisphere tumor is included in the phantom. As indicated in Table III, this object is detected and localized. A smaller S/C ratio is obtained compared to the S/C ratios of 2-D objects, indicating that detection of small 3-D objects will be challenging.

Finally, a 1.2-cm wood dowel tumor in the PVC pipe is imaged with the horn antenna. Results, shown in Fig. 9 and summarized in Table III, indicate that the pipe reflections are reduced and the tumor is successfully detected. As suggested by Table II, the S/C ratio is smaller than the one obtained for the monopole antenna due to the presence of larger reflections from the second pipe interface. The image reconstruction algorithm is designed to reduce reflections from the first pipe interface, as these reflections dominate experimental and simulated results. However, with further adaptation of the image formation algorithm, the reflections from the second pipe interface may be also reduced.

V. Conclusion

In this paper, we have verified the basic concepts employed in the numerical modeling of CMI and established the feasibility of experimental data acquisition in the frequency domain. Inverse chirp-z transforms are found to be a useful tool for transforming data to the time domain, providing improved results when compared to the inverse Fourier transforms. Improved image formation algorithms are tested on a variety of phantoms, showing successful reduction of pipe reflections and detection of 2-D objects. A 3-D object was also detected, however, this result indicates that detection of small 3-D objects is likely to be challenging. Images of two objects placed in close proximity suggest that the system resolution is near the estimated 1.8 cm. This does not imply that the detection limit is on the order of centimeters, as a 3-mm-diameter dowel was successfully detected. Results obtained with the horn antenna appeared promising from the point of view of improved relative tumor response, however the larger reflection from the second pipe interface degrades results. With algorithms tuned to both pipe reflections, clutter reduction may be achieved.

Although promising results are obtained for detection in a 2-D plane encircled by antennas, the ability of the imaging technique to localize objects along the axis of the PVC pipe (or in 3-D) is not explored in this paper. These results may demonstrate improved performance with directional or higher gain antennas. As a next step, experimental scanning with a 3-D cylindrical array and more realistic phantoms (both in terms of shape and properties) is proposed.

Acknowledgment

The authors would like to acknowledge the technical support of A. Low, the invaluable assistance of K. Caputa, University of Victoria, Victoria, BC, Canada, and helpful discussions with Dr. M. Okoniewski and Dr. M. Potter, both of the University of Calgary, Calgary, AB, Canada.

References

[1] S. C. Hagness, A. Taflove, and J. E. Bridges, "Two-dimensional FDTD analysis of a pulsed microwave confocal system for breast cancer detection: Fixed-focus and antenna-array sensors," *IEEE Trans. Biomed. Eng.*, vol. 45, pp. 1470–1479, Dec. 1998.

[2] ——, "Three-dimensional FDTD analysis of a pulsed microwave confocal system for breast cancer detection: Design of an antenna-array element," *IEEE Trans. Antennas Propagat.*, vol. 47, pp. 783–791, May 1999.

[3] X. Li and S. C. Hagness, "A confocal microwave imaging algorithm for breast cancer detection," *IEEE Microwave Wireless Comp. Lett.*, vol. 11, pp. 130–132, Mar. 2001.

[4] E. Fear and M. Stuchly, "Microwave system for breast tumor detection," *IEEE Microwave Guided Wave Lett.*, vol. 9, pp. 470–472, Nov. 1999.

[5] E. C. Fear and M. A. Stuchly, "Microwave detection of breast cancer," *IEEE Trans. Microwave Theory Tech.*, vol. 48, pp. 1854–1863, Nov. 2000.

[6] E. C. Fear, X. Li, S. C. Hagness, and M. A. Stuchly, "Confocal microwave imaging for breast tumor detection: Localization of tumors in three dimensions," *IEEE Trans. Biomed. Eng.*, vol. 49, pp. 812–822, Aug. 2002.

[7] J. G. Maloney and G. S. Smith, "A study of transient radiation from the Wu-King resistive monopole—FDTD analysis and experimental measurements," *IEEE Trans. Antennas Propagat.*, vol. 41, pp. 668–676, May 1993.

[8] R. Formato, "Design wideband antennas," *Electron. World*, vol. 103, pp. 825–829, Oct. 1997.

[9] E. C. Fear, A. Low, J. Sill, and M. A. Stuchly, "Microwave system for breast tumor detection: Experimental concept evaluation," in *IEEE AP-S Symp. Dig.*, 2002, pp. 819–822. invited.
[10] A. Taflove and S. C. Hagness, *Computational Electrodynamics: The Finite-Difference Time-Domain Method*, 2nd ed. Norwood, MA: Artech House, 2000.
[11] *Double-Ridged Waveguide Horn Model 3115 Operational Manual*, Oct. 1998.
[12] B. Ulriksson, "Conversion of frequency-domain data to the time domain," *Proc. IEEE*, vol. 74, pp. 74–77, Jan. 1986.
[13] D. A. Frickey, "Using the inverse chirp-z transform for time-domain analysis of simulated radar signals," in *Proc. 5th Int. Signal Processing Applications and Technology Conf.*, Dallas, TX, Oct. 18–21, 1994, pp. 1366–1371.

Elise C. Fear (S'98–M'02) received the B.A.Sc. degree in systems design engineering from the University of Waterloo, Waterloo, ON, Canada, in 1995, and the M.A.Sc. and Ph.D. degrees in electrical engineering from the University of Victoria, Victoria, BC, Canada, in 1997 and 2001, respectively.

From 2001 to 2002, she was a Natural Sciences and Engineering Research Council of Canada (NSERC) Post-Doctoral Fellow in electrical engineering with the University of Calgary, Calgary, AB, Canada. In July 2002, she joined the same department as an Assistant Professor. Her research interests involve the interaction of electromagnetic fields with living systems, including the interaction of low-frequency fields with biological cells and microwave breast cancer detection.

Jeff Sill (S'02) received the B.Eng. degree in electrical engineering from the University of Victoria, Victoria, BC, Canada, in 2002, and is currently working toward the M.Sc. degree in electrical engineering at the University of Calgary, Calgary, AB, Canada.

His research interests include microwave breast cancer detection and medical applications for digital signal processing.

Maria A. Stuchly (S'71–SM'76–F'91) received the M.Sc. degree in electrical engineering from the Warsaw Technical University, Warsaw, Poland, in 1962, and the Ph.D. degree in electrical engineering from the Polish Academy of Sciences, Warsaw, Poland, in 1970.

From 1962 to 1970, she was with the Warsaw Technical University and the Polish Academy of Sciences. In 1970, she joined the University of Manitoba. In 1976, she joined the Bureau of Radiation and Medical Devices in Health and Welfare, Ottawa, ON, Canada, as a Research Scientist. In 1978, she was associated with the Electrical Engineering Department, University of Ottawa, as an Adjunct Professor. From 1990 to 1991, she was a Funding Director of the Institute of Medical Engineering. In 1992, she joined the University of Victoria, Victoria, BC, Canada, as a Visiting Professor with the Department of Electrical and Computer Engineering. Since January 1994, she has been a Professor and Industrial Research Chairholder funded by the National Sciences and Engineering Research Council of Canada, BC Hydro, and Trans Alta Utilities. Her current research interests are in numerical modeling of interaction of electromagnetic fields with the human body and wireless communication antennas.